Numerical study of fixed Oscillating Water Column with RANS-type two-phase CFD model

Thomas Vyzikas[a,1], Samy Deshoulières[b], Olivier Giroux[c], Matthew Barton[a], Deborah Greaves[a]

[a] *University of Plymouth, School of Marine Science and Engineering, Drake Circus, PL48AA Plymouth, UK*
[b] *Ecole Centrale de Marseille, 38 Rue Frédéric Joliot Curie, 13013 Marseille, France*
[c] *Ecole nationale supérieure des mines de Nantes, 4 Rue Alfred Kastler, 44300 Nantes, France*

Abstract

Various studies investigated the behaviour and the performance of Oscillating Water Columns (OWCs) suggesting many alternative design concepts to improve the efficiency of the device. The OWCs examined here are fixed on the seabed and have a slit opening at the seaward side. The present study investigates the applicability of a multiphase Reynolds Averaged Navier-Stokes (RANS) numerical model for simulating the interaction between an OWC and regular and irregular waves. An initial validation of the open-source computational fluid dynamics (CFD) software package OpenFOAM with the wave generation and absorption toolbox waves2Foam is performed against experimental results obtained at the COAST laboratory of the University of Plymouth. The main aim of the study is to complement to the validation of RANS CFD models and later employ the broadly used numerical tool for further studies for better understanding the behaviour of the OWCs. A method based on mechanical damped oscillations for calculating the eigenfrequency of the device from a decay test is presented and compared with the performance curve. The strength of CFD modelling for obtaining better insight to the hydrodynamics of OWCs is also demonstrated.

Keywords: CFD, OWC, validation, OpenFOAM, waves2Foam,

[1] Corresponding author, Email address: thomas.vyzikas@plymouth.ac.uk

hydrodynamics

---

1. Introduction

Marine renewable energy (MRE) appears to be a viable alternative solution as a carbon-free energy generation method [1], covering a wide range of applications and being able to respond to power demands of remote island communities [2]. Thousands of prototypes have been developed for many decades now for exploiting the energy of the ocean waves, but a consensus to a single economically competitive prototype and reliable is yet to be reached [3].

The best-studied and most successful WEC concept seems to be the OWC technology, which has reached the stage of deploying full scale prototypes in open sea conditions [4] [5]. Floating OWC devices were commercialised in Japan in 1965 and more recently a 1:4$^{\mathrm{th}}$-scale buoy converter was deployed in Ireland [6]. Fixed OWC devices are commonly deployed near the shore in shallow water, where lower wave energy than offshore is available, due to the energy dissipation caused by the bottom friction and wave breaking [7]. This, however, can be mitigated if areas where wave energy is locally focused due to topography are chosen [8]. Nevertheless, near-shore OWCs are not exposed to harsh open-ocean wave conditions and they can be better monitored and maintained, which increases their survivability. Moreover, OWCs embedded in breakwaters or piers can have a dual functionality of energy generation and coastal protection [9], which increases the chances for investing in these projects.

In the present study, a conventional fixed OWC is used as a fundamental model for validating a numerical code. The classic design for OWCs embedded in breakwaters consists of a partially submerged hollow structure which incorporates a water column and an overlying air chamber. The front wall has an opening that allows interaction of the water column with the incident waves. The oscillation of the water inside the chamber of the OWC causes motion of the air, which is forced to pass through a bi-directional air turbine usually placed in a duct on the top of the structure. The turbine is the power take-off (PTO) mechanism used to transform the pneumatic energy into mechanical energy and afterwards to electricity with the use of a generator.

The numerical modelling of OWCs ranges from frequency-domain models [10] [11] to time-domain 1D models [12] or more complicated potential flow models employing Boundary Element Methods (BEM) [13] and high order BEM combined with Eulerian-Langrangian techniques [14]. A review of the different numerical modelling techniques for OWC is available in [15].

The most advanced category of numerical models refers to CFD Navier-Stokes codes, which have high computational cost, but can achieve high accuracy when examining fully nonlinear problems [16]. Nowadays, increasing processing power make these codes applicable for practical engineering problems. Regarding the CFD modelling of OWCs, Teixeira et al. [17] used the RANS model Fluinco with an aerodynamic model and compared the results with the commercial code Fluent. López et al. [18] examined different damping coefficients of the PTO with the RANS numerical model STAR-CCM+. A similar study was performed in REFF3D [19]. ANSYS-ICEMCFD & CFX was employed to examine the effect that geometric changes have on the performance of the OWC [20]. A recent study validated OpenFOAM and IHFOAM [21] for a fixed detached OWC device [22]. A similar detached OWC was simulated in OpenFOAM testing different turbulence models and using boundary conditions from waves2Foam and a piston-type wave maker [23].

Realising the insight into the behaviour and hydrodynamic characteristics of a WEC that CFD modelling can provide, the present study aims to validate the open-source robust CFD code OpenFOAM with the wave generation toolbox waves2Foam [24] for the wave-OWC interaction problem against experimental results produced for this scope [25]. The OWC is examined in regular and irregular wave conditions with and without PTO, herein also mentioned as “lid-on” and “lid-off” OWCs, essentially testing an absorbing sea wall. The validation process of the present study is complementary to previous studies [18] [19] [22] that used similar solvers and examined a wider range of wave conditions. Here, the most challenging part was the high damping of the PTO.

The well-validated numerical wave tank (NWT) was used in the second part of the work for additional investigations, such as the sloshing in the chamber of the OWC and the reflection coefficients of the OWCs. Moreover, numerical results are used to draw the performance curve of the OWC and to shed light in the hydrodynamic and aerodynamic behaviour of the device. A time domain method for calculating the natural frequency of the OWC via a decay test is also demonstrated.

2. Materials and methods

2.1. Description of the solvers

OpenFOAM (Open source Field Operation and Manipulation) is an open-source and freely available CFD package comprising a large set of C++ libraries. The programming in OpenFOAM is efficient thanks to the mimicking of the form of the partial differential equations (PDEs) in the code and to the modularity of the object oriented language [26].

Regarding fluid flows, OpenFOAM can handle 3D domains solving multi-phase flows with several approaches of solving the Navier-Stokes equations with several turbulence models [27]. The free-surface flows are resolved with an advanced two-phase flow technique based on the Volume of Fluid (VoF) method [28]. This technique for simulating free surface problems has great capacity in simulating over-turning flows, wave breaking [29] and green water effects. However, it might suffer from diffusion if the mesh resolution is too low.

In this study, the RANS set of equations was used with a $k - \epsilon$ turbulence model. The standard values of the parameters of the $k - \epsilon$ turbulence model were used: $C_\mu = 0.09$, $C_{1\epsilon} = 1.44$, $C_{2\epsilon} = 1.92$ and $\sigma_\epsilon = 1.30$ [30]. The standard $k - \epsilon$ turbulence model was also used by López et al. [18] in a similar study, while [19] and [22] employed a $k - omega$ and a $k - omega \quad SST$, respectively. The two-equation turbulence closure models have similar range of applicability, with $k - omega$ being more appropriate for adverse pressure gradient problems. A wide variety of turbulence models is readily available in OpenFOAM for more specific studies [30]. The two fluids are considered incompressible and immiscible. The assumption of compressibility holds since the flow is below the subsonic limit, where compressibility effects become important [31]. This is confirmed by the results where the maximum air velocity encountered locally is about 35 m/s, which gives a maximum ratio of flow velocity over Mach number equal to 0.1. The governing equations are solved simultaneously for the two fluids and they can be written as a set of mass conservation equation (Equation 1) and momentum conservation equations (Equation 2) [21],.

$$\nabla \mathbf{U} = 0, \tag{1}$$

$$\frac{\partial \rho \mathbf{U}}{\partial t} + \nabla \cdot (\rho \mathbf{U} \mathbf{U}) - \nabla \cdot (\mu_{eff} \nabla \mathbf{U}) = -\nabla p^* - g \cdot \mathbf{X} \nabla \rho + \nabla \mathbf{U} \cdot \nabla \mu_{eff} + \sigma \kappa_c \nabla \alpha_i \tag{2}$$

Here, $\mathbf{U}$ is the velocity vector, ρ is the density, p^* the pseudo-dynamic pressure, $\mathbf{X}$ the position vector, σ the surface tension coefficient, which is taken equal to zero, κ_c the curvature of the interface, α_i the fluid phase fraction and μ_{eff} the efficient dynamic viscosity. $\mu_{eff} = \mu + \mu_t$, with μ being the molecular dynamic viscosity ($10^{-3} m^2/s$ and $1.4810^{-5} m^2/s$ for water and air, respectively) and μ_t is the turbulent viscosity given by the turbulence model; here, $\mu_t = \rho C_\mu \frac{\kappa^2}{\epsilon}$ [31].

The most commonly used solver for multiphase incompressible flows supplied in OpenFOAM is “interFoam”. The pressure-velocity coupling is achieved with the use of the PIMPLE algorithm, which is a combination of SIMPLE and PISO algorithms [31] [30]. In the simulations presented in this paper, PIMPLE was operating in PISO mode.

The time step in the simulations is adjustable and controlled by the Courant number (C_o) ensuring numerical stability [32]. For the case of multiphase flows, OpenFOAM has an additional time-step controller, called “alphaCo”, which refers to the Courant number around the interface of the two fluids. The time-step is the minimum calculated by C_o and “alphaCo”. This feature can improve the computational efficiency of the simulation without reducing the accuracy of resolving the free water surface.

Regarding the numerical schemes for the discretization of the PDEs, the "Euler" first order, bounded, implicit time scheme was used for the time integration and "Gauss linear corrected" second-order, unbounded, conservative scheme for the Laplacian terms scheme. The gradient terms were discretized with second order Gaussian integration.

2.2. Wave generation and absorption in OpenFOAM

The simulation of waves requires special boundary conditions for wave generation and absorption. The most commonly used libraries in OpenFOAM for coastal and ocean engineering studies are waves2Foam [24] and IHFOAM [21]. Both the libraries are based on the "interFoam" solver and they offer a wide variety of pre- and post-processing tools for the simulation of waves. The main difference between the two is that waves2Foam employs a passive wave absorption method, while IHFOAM has an active correction method to absorb reflections on the boundaries.

In this study, a second order Stokes wave definition [33] is used in waves2Foam for the regular wave generation, allowing the calculation of the position of the free water surface and the velocity components at the inlet boundary at every time step. For irregular wave generation, waves2Foam offers the option of selecting an energy spectrum, based on a theoretical distribution. However, it was preferred to use the so called "combinedWaves" method, which allows greater flexibility. Accordingly, multiple wave components are linearly superimposed on the inlet boundary to form the examined JONSWAP spectrum. A ramp-up time of approximately one wave period was used in order to account for the smooth transition of the waves in still water. This follows the same practice as in the experiments [25].

Regarding the absorption of the waves, waves2Foam uses dissipation layers, called relaxation zones. The solution in the relaxation zone is a weighted combination of the RANS solution in the domain and the linear solution based on the boundary definition (target). Equation 3 [24] refers to the calculation of a value of any flow variable ϕ in the relaxation zone. The air-phase velocities in the relaxation zone are set to zero.

$$\phi = \alpha_R \phi_{computed} + (1 - \alpha_R)\phi_{target} \quad (3)$$

with α_R a weighting factor dependent on location in the relaxation zone.

The length of the relaxation zone determines its efficiency. Usually, long relaxation zones provide better absorption, but they also increase the computational cost, while decreasing the effective length of the fully nonlinear domain. Additionally, the relaxation zone has to be sufficiently far from the device in order to allow it to interact freely with the waves.

2.3. Characteristics of the NWT

As the computational cost of CFD simulations is significant, it was decided to use a shorter numerical flume compared to the physical one, which was 28m [25]. The physical flume of the COAST laboratory is equipped with an absorbing piston-type wave paddle and the acquisition of the water level and pressure had a sampling frequency of 128 Hz. The geometric characteristics of the OWC presented here are based on the U-OWC suggested by Boccotti [34]. The NWT was at exactly the same scale as the physical flume, but the OWC was located at 9 m away from the inlet boundary. A schematic of the physical and the numerical wave flume is shown in Figure 1. The OWC occupies the entire width of the flume and it comprises three identical independent chambers, each with an orifice centrally located at the top wall.

Since the OWC was located at one end of the NWT, the outlet relaxation zone was omitted. The total length of the domain is related to the minimum required length of the inlet relaxation zone for absorbing the reflected waves adequately. In preliminary tests, it was found that a relaxation zone of 3m can absorb most of the reflected wave energy and it allows enough space in the nonlinear domain for the wave-OWC interaction. It should be noted that the former selection depends on the wavelength of the input wave. According to sensitivity tests on relaxation zones [24], the reflection coefficient of the 3 m relaxation zone and the regular wave used for the validation (see Section 3.1) is 0.5%. The wavelength of this regular wave was 5.20 m and essentially one wavelength of fully nonlinear domain was left for the wave-OWC problem. The computational cost of a longer high-resolution 3D domain was not manageable and taking into account the good performance of the relaxation zone, that was considered a good compromise between computational cost and accuracy.

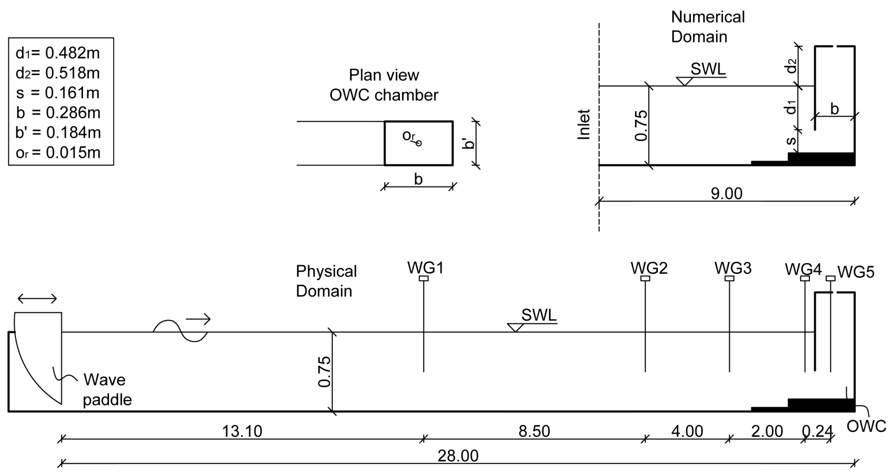

Figure 1: Schematic of the physical and the numerical wave flume, dimensions in (m).

The initial computational domain was three-dimensional and it included all the three chambers of the device. After the preliminary tests, it was decided to use only the central chamber for the sake of saving computational resources, since the behaviour of the chambers was similar. This was also justified by the analysis of the experimental results [25]. The left and right boundaries of the truncated NWT are treated as frictionless walls.

The implementation of the OWC model in the computational domain was achieved with the utility of OpenFOAM "snappyHexMesh", which is an algorithm that refines the background computational cells around a predefined geometry using quadratic refinement. Moreover, "snappyHexMesh" was used to refine the region around the free surface, so that the interface of the two fluids is better resolved, and an area at the vicinity of the OWC, where the flow is complex. After examining different parameters of the refinement, it was decided to use two levels of refinement and six buffer layers, in order to achieve smooth transition between the layers. Figure 2 shows the resulting computational mesh in the vicinity of the OWC and the refined region around the free surface. An extra refinement was applied near the orifice in order to resolve better the fast air flow through this small opening, which occupies 0.35% of the plan area of the chamber (Figure 3). This local refinement allowed the 15 mm diameter circular orifice to be discretized with 6 computational cells in diameter. For comparison, the orifice opening in other numerical studies was much greater varying from 2.7% - 14.7% [22], 0.78% - 7.8% [19] and 0.78% - 3.91% [18]. The induced high damping results in high pressure, which makes the present study more challenging. For the cases that no PTO was considered, the top-wall of the OWC was removed and atmospheric pressure was allowed in the OWC. No-slip and "zeroGradient" boundary conditions are defined on the walls of the OWC for the velocity and the phase fluid fraction, respectively.

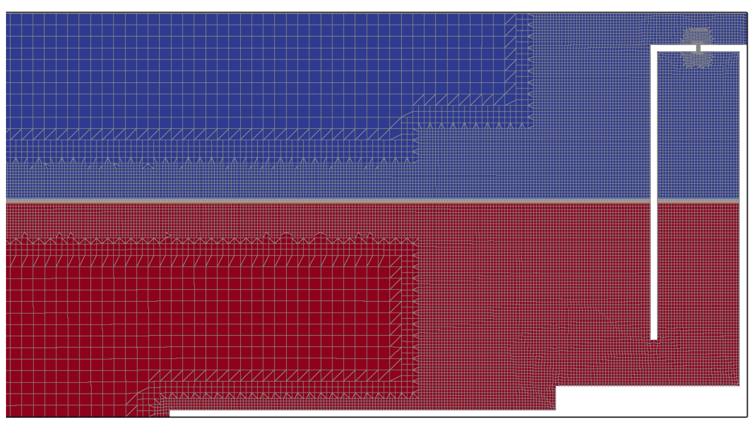

Figure 2: Vertical cross-section of the computational mesh at the vicinity of the OWC, depicting the different regions of refinement. Red and blue colours represent the water and air phase, respectively.

On achieving accurate and grid independent numerical simulations, system-

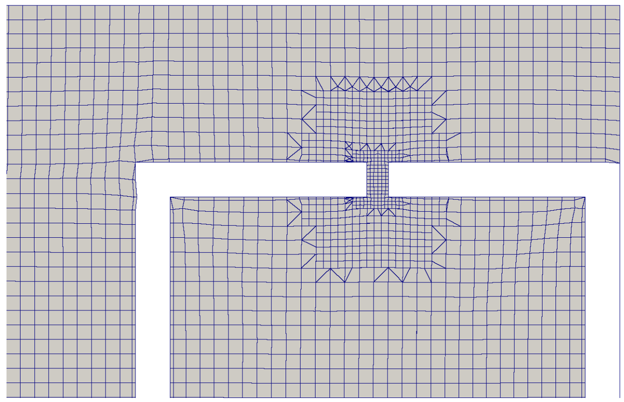

Figure 3: Local refinement of the computational mesh near the orifice of the OWC.

atic convergence tests were conducted. Cubic cells were used, since they are recommended when applying “snappyHexMesh” [27] and because they give more accurate results for highly distorted interface [24]. Two values for the Courant number were used: a high value of $C_o = 1$ and a lower value of “alphaCo”. This allows the water phase to be always very well resolved and it does not cause a significant decrease of the timestep when high velocities occur at the orifice. For the cases without the PTO, alphaCo $= C_o = 0.2$. For the sake of brevity only three tests close to convergence are presented in Figure 4 for the time series of the surface elevation inside the chamber that refer to the OWC without the PTO and are conducted at a preliminary level to select the resolution of the background mesh. Having selected the background mesh, thorough convergence was performed separately for the OWC with the PTO, testing the range of the refined areas, the levels of refinements and the sensitivity to $C_o = 1$ and “alphaCo”. The characteristics of the mesh are presented in Table 1 in the form of $M \times C$, with M being the cell size of the background mesh in cm and C the value of “alphaCo”. It can be seen that the highest resolution (*R3*) and the low resolution cases (*R1* and *R2*) are very similar with an average error of 2% relative to the wave height, with discrepancies appearing only locally. The computational cost of *R3* is almost double than that of *R1* and *R2* and Figure 4 does not justify its selection for the scope of the present study. Since the coputational cost of *R1* and *R2* was similar, it was decided to use the resolution with the lower "alphaCo" (*R1*) for preventing any potential discrepancies when simulating irregular waves. This selection resulted in an 1 million-cell mesh.

	R1	*R2*	*R3*
Resolution	4x0.2	4x0.25	3x0.2

Table 1: Characteristics of the background mesh for the convergence tests. Cell size in cm x alphaCo.

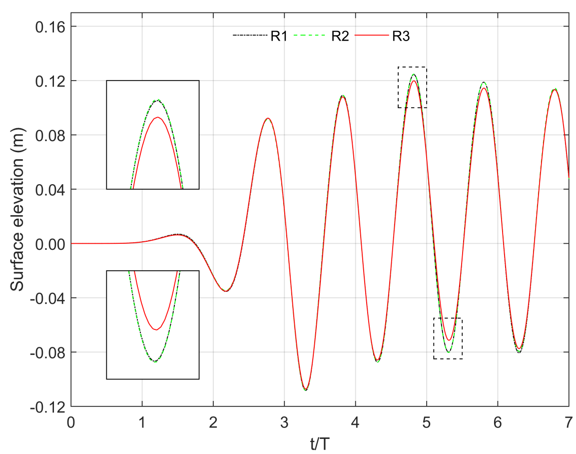

Figure 4: Mesh convergence test for the OWC "lid-off" tested. The time series of the surface elevation are recorded in the central chamber of the OWC.

All the numerical tests were simulated in parallel with Intel Xeon E5-2650 processors at 2.6GHz with OpenFOAM 2.1.1. The presence of PTO increases the computational cost by at least one order of magnitude compared with the "lid-off" cases that require approximately 100 core-hours for 30 s of simulation.

3. Validation

For the regular wave, the validation was performed for the timeseries of the surface elevation inside the OWC and the pressure in the OWC for the cases with the PTO. For the irregular wave, integrated parameters were compared with the experiment, such as the capture width, the energy density spectra of the response of the OWC to the incident sea state and reflection coefficient.

3.1. Regular wave

The wave characteristics used as input to the numerical model were determined from the experimental results by analysing the recorded surface elevation in a time window after the ramp-up time of the wave paddle and before the occurrence of reflections from the OWC, as seen Figure 5a. In this figure, part of the experimental surface elevation at WG1 is presented in comparison with the numerical signal at the inlet boundary. A wave height of $H = 0.088$ m and a wave period of $T = 2.15$ s was used. This wave was found in experiments to be close to the resonant frequency of the device and to have similar behaviour in each of the three chambers [25].

The comparison between the experimental and the numerical results inside the chamber when the PTO is absent is presented in Figure 5b. The frequency of the oscillation is very well resolved, apart from some minor discrepancies at the beginning that might be caused from the ramp-up time of the wave maker. The amplitude of the oscillation is also very well captured, leading to an almost excellent overall comparison. For quantifying and better evaluating the comparison between the physical and the numerical results, the mean average error (MAE) is used, which is calculated according to Equation 4.

$$MAE = \frac{mean(|\eta_{extr}^{exp} - \eta_{extr}^{num}|)}{\alpha^{exp}} \tag{4}$$

where η_{extr} refers to the local extrema and α to the wave amplitude, taken as half of the wave height for simplicity.

It was found that for the "lid-off" case the error is 5.7% of the height of the oscillation, corresponding to 2 mm. This is relatively close to the accuracy of the repeatability of the physical flume (1 mm) [25]. Considering that, it can be safely concluded that the numerical model can replicate an OWC without a PTO with great accuracy.

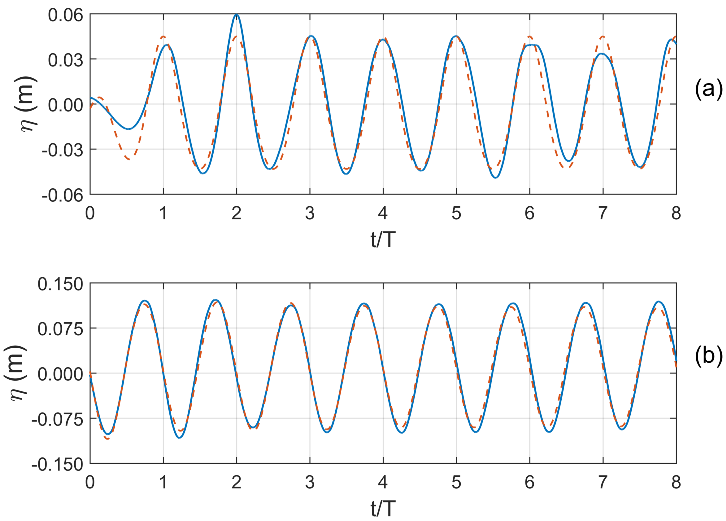

Figure 5: Surface elevation time series upstream of the device (a) and inside the chamber (b) of the model without PTO (- laboratory measurements, - - numerical results).

The comparison between the experimental and the numerical results in the presence of the PTO are shown in Figure 6a for the surface elevation and in Figure 6b for the air pressure inside the chamber of the OWC. The frequency of the oscillation is again very well resolved. The surface elevation in the numerical is also in very good agreement with the physical results, with a MAE of only 6.9%. On the other hand, the pressure shows higher discrepancies than the surface elevation, which eventually causes a different result in the capture width, which is increased compared to the physical model from 0.43 to 0.44.

The study of the device with a PTO includes additional complications related to the air phase, which cause the discrepancies in the pressure. Preliminary studies showed that small fluctuations in the surface elevation can result in significant differences in the air pressure. The accurate calculation of the pressure is challenging for numerical studies and there are commonly discrepancies when comparing with experiments, as observed in previous works [22] [18] [19]. One of the possible reasons that causes discrepancies in the surface elevation can be

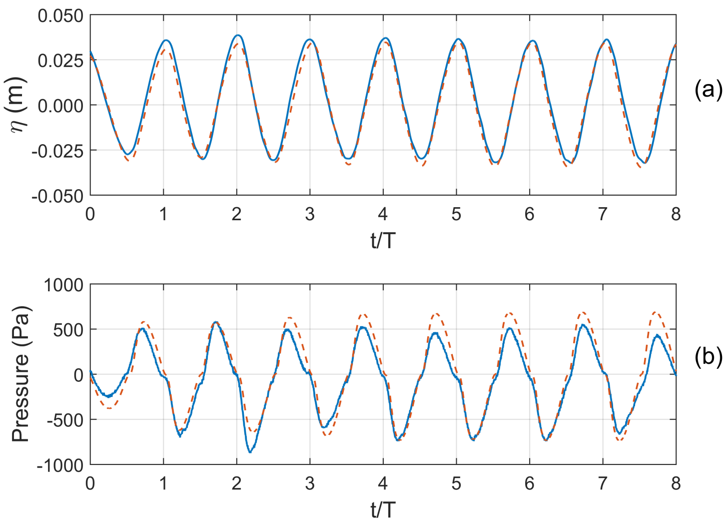

Figure 6: Surface elevation (a) and pressure (b) time series inside the chamber of the model with PTO (- laboratory measurements, - - numerical results).

the re-reflected wave from the inlet relaxation zone that effectively increased the energy of the incident wave as time passes. Evidence for the influence of the re-reflections can be seen from Figure 6b where the pressure gradually increases with time. Before the appearance re-reflected wave ($t/T < 3$) the MAE of the pressure is 7.1% of the maximum pressure difference in one period, while it reaches 14.7% when the re-reflected wave appears. It was observed that when the length of the inlet relaxation was increased, the reflected wave was better absorbed, but the computational cost was greatly increased, due to the added computational cells and the additional equations solved for the target solution of the flow variables at each cell (see Equation 3).

Other reasons that might cause the experimental pressure to be lower than the numerical predictions might be associated with imperfections in the manufacturing of the physical model or with the inherited limitations of the numerical model. As mentioned in Section 2.1 the model solves the incompressible Navier-Stokes equations, which is an accurate approximation for the water phase, but it might not be the case for the air phase. The compressibility of the air phase might influence the results especially when rapid pressure fluctuations are encountered.

In recent work with OpenFOAM and IHFOAM, it was also observed that the pressure in the numerical model was slightly over-predicted [22] when RANS equations were solved. On the other hand, when a LES model was used, the numerically predicted pressure was closer to the experimentally measured pressure [35]. In other studies, the correlation between the experimental and the numerical results is similar to the present study, however the pressure fluctuations were 80 Pa [22], 180 Pa [18], 200 Pa [35] and 900 Pa [19], which are significantly smaller in comparison to 1400 Pa which is observed here. The reason for the high pressure is the high damping induced from the small orifice in combination with the high waves.

All in all, the results of Figure 6 demonstrate that the model performs sufficiently well when a PTO of high damping is present. This is further supported by the fact that the capture width differs only by 2.3% between the physical and the numerical model (0.43 and 0.44 respectively). However, further validation can be useful to identify the source of the discrepancies in the pressure observed here. Taking into account previous works [18] [19] [22], it can be concluded that a RANS-VOF model performs sufficiently well for OWC simulations.

3.2. Irregular wave

The irregular wave tested in the numerical model is based on a JONSWAP spectrum with $H_s = 0.045$ m and $f_p = 0.465$ Hz. The phases were selected by a random number generator that created random phases uniformly distributed between 0 rad and 2π rad. The spectrum is discretized by 200 wave components with equidistant frequencies and a low and high cut-off frequency of $0.3f_p$ and $3f_p$, respectively. The time of the simulation was selected such that all the components were present in the NWT and the shape of the spectrum was properly retrieved at any location in the tank, finding that 157 s is sufficient for that. The computational cost of simulating a 3D OWC with a PTO in irregular waves is about 25K core hours, posing a serious limitation to the cases that can be examined.

In order to evaluate the numerical results, the same techniques for smoothing the spectrum [36] and reflection analysis [37] were used, as for the experimental results [25]. The original signal was separated into 8 segments and a method similar to Welch method without overlapping was used. This method is described in [36] and results in a smoother spectrum in the expense of lower frequency resolution. If p_n segments are selected, the frequency resolution of the spectrum is reduced by p_n times, yielding an error of this process of $\frac{1}{p_n}100\%$. The optimal number of segments is selected by trials. The reproduction of the irregular wave in the NWT is examined in Figure 7. It is shown that in the numerical model the incident energy density spectrum retrieved after the reflection analysis in the middle of the NWT is in very good agreement with the input JONSWAP spectrum. In the experiment, the only WGs available for the reflection analysis were $\Delta x = 4.0$ m apart, which is not an indicated distance for separating the phases of the incident and reflected waves. However, as shown here, reflection analysis can be used to retrieve the incident energy spectrum. The applicability of the reflection analysis was tested in the numerical model between WGs that were close to each other ($\Delta x = 0.2$ m), as the common practice suggests, and farther apart at a distance of $\Delta x = 3.0$ m, after the end of the relaxation zone and sufficiently away from the device. It is demonstrated that the shape and energy of the spectrum are very similar regardless the distance between the WGs, giving confidence that reflection analysis can be applied to obtain the incident spectrum even when the WGs are far apart. Similar results were obtained for different distances between the WGs varying from 0.1 m to 5.0 m with the numerical model at preliminary tests. The recommended distances between the WGs for the reflection analysis are discussed by Goda & Suzuki [38], as well as the possibility of divergence and the distance of the closest WG to the reflective structure. In our case, divergence is expected at 0.3 Hz, where there is not high energy content and WG3 is far enough from the OWC, in order to prevent any discrepancies in the recordings caused by the reflective structure. The measured spectra after the reflection analysis in Figure 7 are not exactly the same with the input spectrum, because in a random process of irregular wave generation and propagation the behaviour of the numerical and the experimental tank is expected to be different. For the conditions tested, the experimental spectrum had a lower peak and greater spread of energy to high frequencies.

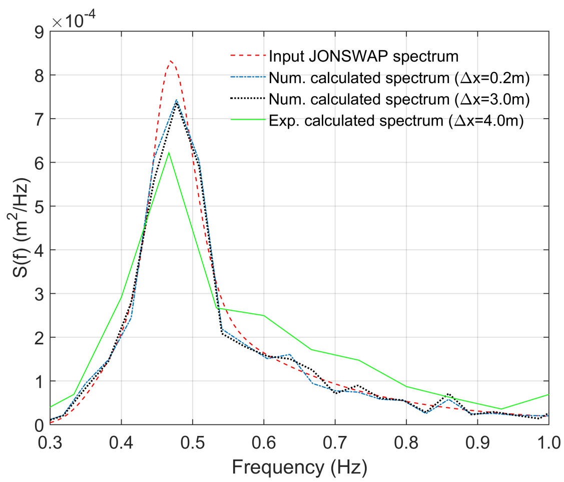

Figure 7: Comparison between the experimental and the incident spectra calculated with the reflection analysis for different distances between the WGs in the NWT.

Since the time series of the surface elevation is random, only the capture width and the spectrum inside the chamber of the OWC can be considered for the validation. The capture width in the numerical model has a value of 0.42, which is close to that measured in the experiment (0.41). The difference between the two is only 2.4%, which is considered good agreement. The comparison of the energy density spectra inside the OWC in Figure 8 shows that the response of the OWC to the incident irregular sea is similar between the numerical model and the experiment, both for the cases when the PTO is present (Figure 8a) and when the PTO is absent (Figure 8b). Figure 8c shows the spectrum of the measured pressure inside the central chamber of the OWC in the experiment and compares it against the numerical model results for the model with the PTO. Good agreement is observed, but the differences are greater compared with the spectra of the surface elevation. As demonstrated for the regular waves, small differences in surface elevation in the OWC result in augmented differences in the pressure, especially in the case for PTO with high damping. Nevertheless, any discrepancies can be readily attributed to the differences between measured incident spectra in the physical and numerical flumes and to a lesser extent to the decreased frequency resolution. Using the exact measured spectrum from the physical flume is expected to minimize these discrepancies, however in many cases, such as field and hindcast data the phases are not known.

In conclusion, together with previous validations using two-phase RANS numerical models [18] [19] [22], it was demonstrated that the NWT designed in OpenFOAM and waves2Foam can adequately replicate the complex phenomenon of wave-OWC interaction and it can be used for further studies. Despite the good performance of the NWT for the OWC with and without PTO in regular and irregular waves, the validation section indicates that there are still issues that require further efforts in order to be addressed. The imperfect absorption of the reflected waves from the inlet can cause considerable pressure discrepancies in the OWC and the study of irregular waves should be performed in a more computationally efficient way in order to be able to examine the effect of random phases on the response of the OWC.

4. Further numerical studies

The first part of the paper dealt with the validation of the NWT for the wave-OWC interaction problem. The present study contributes to further validate the RANS-VOF NWT that was used in similar previous studies [18] [19] [22]. The validated numerical model is used in the following part of the paper to examine the sloshing in the OWC chamber, the reflected waves from the OWC and to determine the resonant frequency of the OWC with a performance curve and a decay test. Insight into the hydrodynamics and aerodynamics of the OWC is provided at the end of this section.

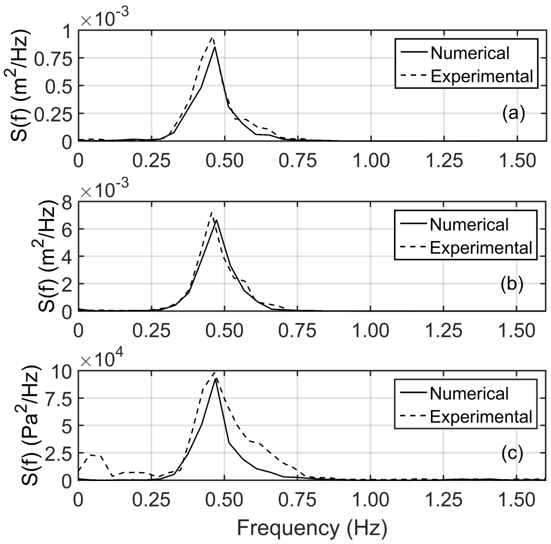

Figure 8: Comparison between the measured energy density spectra inside the OWC with the PTO (a) and without the PTO (b) in the experiment and numerical model. Comparison of the pressure spectrum inside the central chamber (c).

4.1. Sloshing and other distrurbances in the chamber

For all the results presented until now, the free surface elevation inside the chamber was measured by a single wave gauge located in the centre of the OWC. However, under certain conditions, an internal lateral wave can appear in the chamber, which is commonly referred to as sloshing. Sloshing occurs under certain conditions that depend on the wavenumber K and the width of the OWC b. According to [39], the first mode of the standing wave (sloshing) occurs when $Kb = \pi$. For the OWC examined here, this corresponds to wave frequency of 1.65 Hz. Therefore, sloshing is not expected for the wave conditions tested throughout the paper. Despite that, there might be other disturbances of the flow, for example vortices caused from the lip of the front wall or reflected waves from the back wall that are partially trapped in the chamber. Such an effect is visible in Figure 6d and Figure 11 in [40], where it is argued that the internal disturbances are caused by sloshing, but this is not justified based on the geometry of the OWC and the waves tested. However, it is clear that these effects can alter the performance of the OWC and give a false picture of the water motion in the chambers, if this is measured at one location only [40].

To ensure that there is no sloshing or other disturbances of the free water surface in the OWC, four wave gauges were added close to each corner of the chamber. The comparison of the results revealed a maximum difference of 0.2% relative to the wave height among the WGs. Practically, the effect of any spurious oscillations in the OWC is negligible and the use of a single wave gauge was sufficient for the present study. It can be argued that the high draught of the front wall of the OWC facilitates a piston-type movement of the water column inside the device, which limits any disturbances at the free water surface.

4.2. Reflection analysis

The evaluation of the behaviour of OWCs should include additional parameters apart from the performance, since the devices might be located in operational breakwaters and piers. The results of the reflection analysis [37] of the OWCs are compared with a fully reflective vertical wall, tested at the exactly the same conditions in the NWT and located at the same place of the front wall of the OWC. The numerical reflection coefficient is also compared with that obtained from the physical model tests.

The reflection coefficient is calculated as the ratio of the difference between the total and incident energy with the incident energy. The energy of the spectra is calculated as the integral of the variance energy density. All measurements are taken in the middle of the NWT, where additional WGs are placed, sufficiently away from the device and the inlet relaxation zone, so that the results remain intact from the local distortions.

The results presented in Figure 9 show the theoretical input spectrum, the incident calculated wave spectrum from the reflection analysis and the total measured spectrum for a vertical wall (a), OWC "lid-off" (b) and OWC "lid-on" (c). As seen that the theoretical and calculated incident spectra are similar. The reflection coefficient of the vertical wall was calculated at 97%, while it was only 39% and 46% for the OWC without and with PTO, respectively. The experimental reflection coefficient were calculated at 30% and 34% for the "lid-off" and "lid-on" case, respectively, which are similar to the numerical values. The agreement is satisfactory, especially taking into account the randomness of the wave field.

It can be seen that the employment of an OWC in a breakwater can potentially limit the reflected waves in comparison with a vertical breakwater and can create a calmer wave field for navigation.

4.3. Performance curve

One of the most crucial aspects in the examination of an OWC is to determine its resonant frequency in order to be able to tune it to the incident waves and increase its hydrodynamic efficiency. In this section, the OWC with the same PTO of 15 mm diameter is tested under various regular waves with frequencies varying from 0.36 Hz to 1 Hz and constant wave height of 0.03 m, in order to derive its performance curve. This is done with the calculation of the capture width C_w for every test, as a ratio of the absorbed power of the OWC

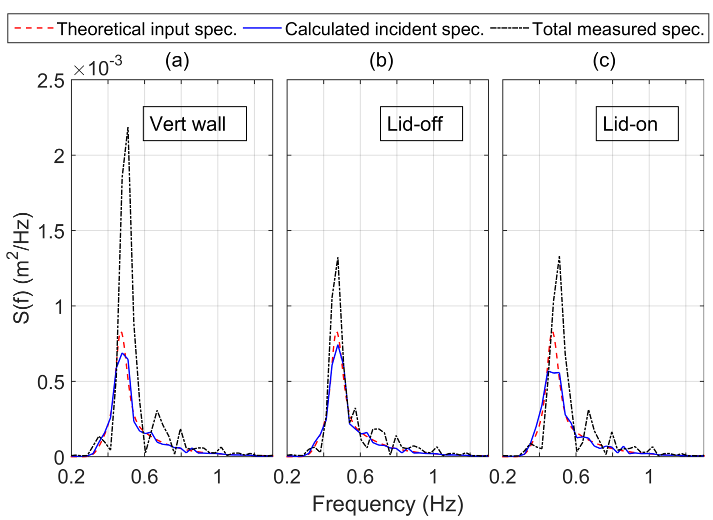

Figure 9: Frequency spectrum of the free surface elevation at 4.5 meters in front of the front wall of the OWC and the vertical wall breakwater.

over the incident wave power per meter length of the OWC [41].

Figure 10 shows the performance curve for different dimensionless wave numbers (Kh), which is defined from the linear dispersion relation as $\omega^2/g = Ktanh(Kh)$, where $\omega = 2\pi f$, with f being the frequency of the wave in Hz, h is the water depth and K the wavenumber. The present results are compared with the experimental study of Morris-Thomas [42], the analytical study of Evand & Porter [39] and the numerical study of Zhang, et al. [40] (case C of high draught). To allow an easier evaluation of the results, the points of each study were fitted with a fifth order polynomial curve.

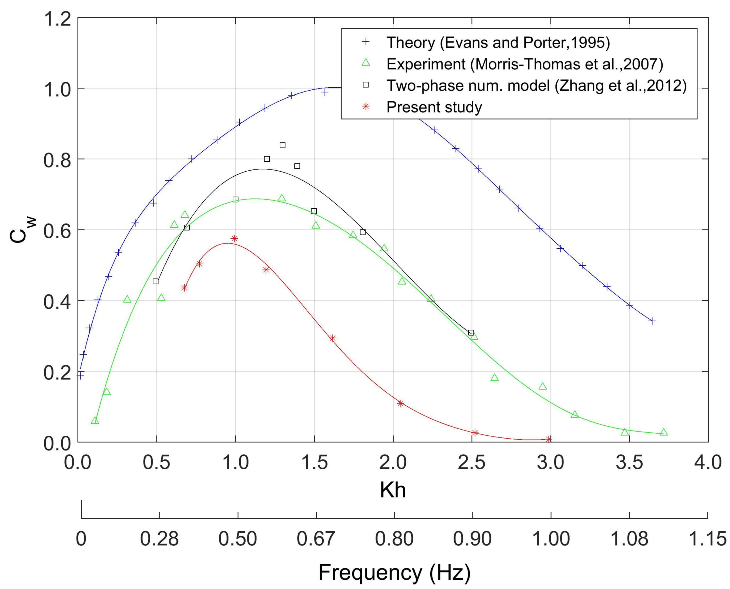

Figure 10: Performance curve presented as the hydrodynamic efficiency versus dimensionless wave number and the frequency of each regular wave tested.

It can be seen in Figure 10 that the present study has a peak of performance at around $Kh = 1$, corresponding to $f = 0.50$ Hz, and a maximum capture width of $C_w^{pres} = 0.57$. On the other hand, Zhang's numerical tests and Morris-Thomas' experimental tests have a peak performance at around $Kh = 1.2$ and a capture width of $C_w^{Zh} = 0.68$ and $C_w^{MT} = 0.76$, respectively. The low capture width of the present study can be explained by the high damping of the model and different geometric parameters. Very low frequency waves ($Kh < 0.5$) could not be tested in the present NWT, since they have a disproportional wavelength to the length of the numerical flume, causing standing waves.

The biggest disadvantages of the performance test are the requirement for many simulations with regular waves and the long NWT needed for testing low frequency waves.

4.4. Decay test

The decay test is an alternative method for determining the resonance frequency of a device by imposing initial conditions to the system and then to let it respond freely. Contrary to the performance curve, this method needs only one test which can save a lot of computational resources. This method is commonly used for floating bodies [43], but rarely for fixed OWC. A similar approach to the present one for performing a decay test with a fixed OWC was presented recently [35], where the FFT of the time series was used to determine the resonant frequency of the device. Here, the theory of mechanical vibrations with viscous damping is employed.

To perform the decay test in the NWT, the free surface elevation inside the device was set at 0.15 m higher than the still water level (SWL) and then, the system was released to respond freely in the absence of any incident waves. The time series of the surface elevation inside the OWC is shown in Figure 11 for the "lid-off" and the "lid-on" case.

Lid-off case

Assuming that the OWC is a system with a linear viscous damping behaviour, the decay test can be used as a time response method to determine the damping of the system and estimate the natural and resonant frequency. The Logarithmic Decrement Method (LDM) is employed, which holds for single degree of freedom oscillatory underdamped motions [44]. According to LDM, when a system with viscous damping is excited, it decays based on Equation 5.

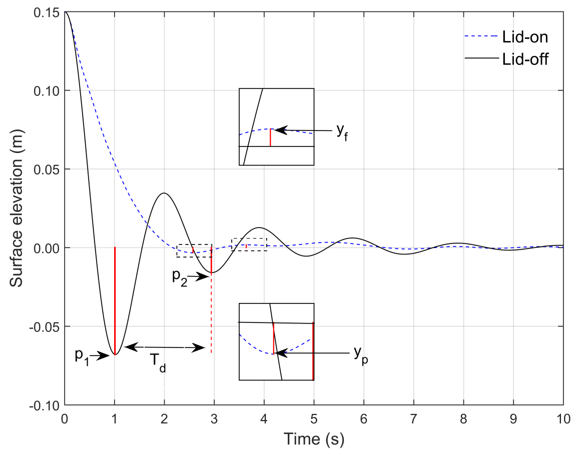

Figure 11: Time history of the surface elevation in the centre of the central chamber for the "lid-off" and "lid-on" cases used for the decay test.

The ratio between two amplitudes separated by r number of periods is defined as the logarithmic decrement δ (Equation 6).

$$y(t) = y_0 e^{-\zeta\omega_n t} sin(\omega_d t) \tag{5}$$

where $y(t)$ is the response of the system, y_0 the initial excitation (here, 0.15 m), ω_n the undamped natural frequency, ω_d the damped natural frequency and ζ the damping ratio.

$$\delta = \frac{1}{r} ln\left(\frac{y(t)}{y(t + rT_d)}\right) \tag{6}$$

where T_d is the period of the damped response given as $T_d = 2\pi/\omega_d$ (see Figure 11).

The damped natural frequency (ω_d) is related to the undamped natural frequency (ω_n) and damping ratio (ζ) as:

$$\omega_d = \sqrt{1 - \zeta^2}\omega_n \tag{7}$$

Substituting Equation 5 and Equation 7 to Equation 6 for two successive peaks p_1 and p_2 $(r = 1)$, as seen in Figure 11, yields:

$$\delta = ln(e^{\zeta \frac{\omega_n}{\omega_d} 2\pi}) = \frac{\zeta}{\sqrt{1-\zeta^2}} 2\pi \tag{8}$$

For an underdamped oscillation $(\zeta < 1)$ the damping ratio is expressed as:

$$\zeta = \frac{1}{\sqrt{1 + (\frac{2\pi}{\delta})^2}} = \frac{1}{\sqrt{1 + (\frac{2\pi}{ln \frac{p_1}{p_2}})^2}} \tag{9}$$

The resonant frequency ω_r for a damped oscillation with sinusoidal excitation force is given as:

$$\omega_r = \sqrt{1 - 2\zeta^2} \omega_n \tag{10}$$

It should be noted that $\omega_r < \omega_d < \omega_n$.

Applying the quantities measured from Figure 11 into Equation 7-10 and taking into account that $f = \omega/2\pi$, the resonant frequency f_r is found. All the parameters are summarized in Table 2.

	p_1 (m)	p_2 (m)	ζ	T_d (s)	ω_n (rad/s)	f_r (Hz)
Lid-off	0.067	0.016	0.226	1.950	3.308	0.499

Table 2: Parameters calculated for the decay test for the "lid-off" case.

Lid-on case

The time series of the decay test in Figure 11 for the "lid-on" case show that the decay test for the OWC with the PTO is almost a non oscillatory response, which corresponds to critical damping $(\zeta = 1)$. However, according to the curves for various damping ratios [44], ζ appears to be between $0.5 < \zeta < 1$. If LDM is applied also here, it gives $\zeta = 0.577$, $\omega_d = 1.74$ rad/s and $f_r = 0.196$ Hz. This is an unrealistic result, which is caused due to the fact that the accuracy of LDM decreases as ζ increases past 0.5.

For damping ratios $0.5 < \zeta < 0.8$ the Method of Fractional Overshoot (MFO) is commonly applied [45]. The fractional overshoot OS is given as:

$$OS = \frac{y_p - y_f}{y_f} \tag{11}$$

where y_p is the amplitude of the first peak of the step response and y_f is the settling amplitude (see Figure 11).

The damping ratio is then related to OS as:

$$\zeta = \frac{-ln(OS)}{\sqrt{\pi^2 + ln^2(OS)}} = \frac{1}{\sqrt{1 + (\frac{\pi}{ln(OS)})^2}} \tag{12}$$

The time of the local maxima and minima is given by:

$$t = \frac{n\pi}{\omega_n \sqrt{1 - \zeta^2}} \tag{13}$$

For $n = 1$ the time of the first peak:

$$t_p = \frac{\pi}{\omega_n \sqrt{1 - \zeta^2}} \tag{14}$$

The settling time, which is the time required for the transient oscillation to reach the steady-state within $\pm 2\%$ of its value is approximated as:

$$t_s = \frac{4}{\omega_n \zeta} \tag{15}$$

Ideally, if the damping is not very high, y_p and y_f represent distinct values in the decay graph and OS can be evaluated in a straight forward manner. However, in the present case y_p is already almost within $\pm 2\%$ of the settling value, i.e. 0.003 m, which brings the MFO to its limits of applicability. The values of the settling time and the time of the first peak can be estimated from Figure 11, which are found as $t_s = 2.701$ s and $t_p = 2.585$ s, respectively. Substituting these values in Equations 14 and 15 results in a system with two unknowns: ζ and ω_n. The solution yields $\zeta = 0.773$ and $\omega_n = 1.916$ rad/s. The natural frequency is calculated as $f_n^d = 0.305$ Hz. Resonance frequency for this case is not defined. It can be seen from the value of ζ that the PTO induces very high damping. All the parameters are summarized in Table 3.

	t_p (s)	t_s (s)	ζ	ω_n (rad/s)	f_n^d (Hz)
Lid-on OWC	2.585	2.701	0.773	1.916	0.305

Table 3: Parameters calculated for the decay test for the "lid-on" case.

The damped natural frequency found with the decay test for the "lid-on" OWC is $f_n^d = 0.305$ Hz, which compares well with the RAO of the surface elevation for the "lid-on" case (see Figure 5 [25]), where the surface elevation resonance appears to be below 0.400 Hz. The resonance frequency found from the decay test for the "lid-off" OWC is $f_r = 0.499$ Hz, which is very close to the peak of the RAO of the physical model (Figure 5 in [25]) estimated at 0.470 Hz and at the same time practically identical to the peak of the performance curve in Figure 10 estimated at approximately 0.500 Hz.

Applying a FFT analysis on the time series of the decay test presented in Figure 11, reveals the response of the OWC in the frequency domain. As it can be seen from Figure 12 the OWC with the PTO does not exhibit a resonant frequency, while the OWC without the PTO shows resonance close to 0.500 Hz.

Practically, the small difference between the resonant frequencies calculated from the decay test without the PTO, the response amplitude operator (RAO) and the performance curve gives great importance to the decay test, since it requires only one simulation of few seconds to find with relatively good accuracy the resonance frequency of the OWC. On the contrary, the RAO and the performance curve method require many and relatively long simulations. Employment of the decay test can reduce the range of the frequencies required for the performance curve and save significant computational effort.

The present results demonstrate that when the damping is not high allowing the system to oscillate ("lid-off" case), the resonant frequency of an OWC can be calculated from the commonly used LDM. When the damping induced by the PTO is very high and the system practically does not oscillate, the MFO can

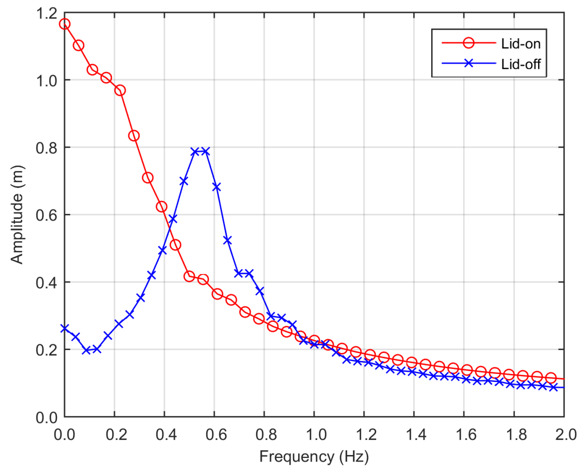

Figure 12: Frequency response of the decay test for the “lid-on” and “lid-off” OWC.

provide a first approximation of the resonant frequency, in order to decrease the range of the frequencies to test for the performance curve. The MFO can also be considered as a good alternative to LDM, when the damping of the system is high, but still the system oscillates and it has not settled before the first peak of the oscillation.

4.5. Hydrodynamic behaviour

The greatest advantage of a CFD model is that it can offer high density information about the flow properties at any time and location in the computational domain. In this section, the numerical results for the regular wave are presented at eight characteristic time instances during a wave cycle, as shown in Figure 13, where the surface elevation in the chamber of the OWC is presented, together with the relative pressure, defined as the difference between the recorded and the atmospheric pressure.

The numerical model outputs for these characteristic time instants are presented in Figure 14. In this figure, the magnitude of the velocity of the two fluid phases is plotted together with the direction vectors for the water phase in a vertical plane that passes from the middle of the OWC and it is normal

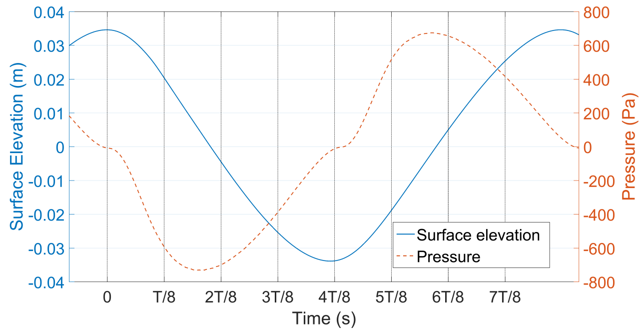

Figure 13: Timeseries of the surface elevation (- blue) and relative pressure (- - red) inside the OWC chamber at eight characteristic time instances during one wave period, marked with vertical lines.

to its front wall. The vertical profile of the horizontal velocity under the front wall of the OWC is presented as well. For convenience, the vertical and horizontal frame of the graphs represent the distance from the SWL and the wave paddle, respectively. The velocity in the air phase is two orders of magnitude higher than that of the water phase, which is expected as the air is accelerated through the orifice. Because of the significant difference between velocity magnitudes in air and water, the two fluid phases are plotted separately. This also explains why different values for C_o and "alphaCo" were chosen in the NWT (see Section 2.1).

It can be clearly seen that the water flow near and in the OWC is complex with stagnant regions or regions of violent jet-type flow (2T/8) and local vortices (6T/8). Perhaps, the most important location is that of the front wall opening that controls the inflow and outflow in the OWC. It can be seen from the horizontal velocity profiles plotted next to the velocity field graphs that the flow is far from a uniform distribution and only part of the opening is active. Moreover, for the first half of the wave cycle (0-3T/8), there is a net outflow from the OWC, until the next incident wave arrives (4T/8) and water flows again into the OWC chamber increasing the surface elevation.

The air motion is also very complex with circulations dominating inside the chamber when the pressure is close to zero (0 and 7T/8) or when the OWC is "exhaling" (5T/8-6T/8). In the latter case, the air flow is stronger near the walls and directly under the orifice. On the other hand, when the pressure drops below zero in the OWC (T/8 to 3T/8) a violent jet-type flow of air enters through the orifice and spreads until it meets the interface with the water. A significant amount of turbulence is expected in the air phase. The present results can be compared with those presented for a detached OWC where the maximum vertical component of the velocity at the orifice was computed at 3 m/s [22] and 15 m/s [23], while here it reached around 30 m/s, indicating the high damping of the PTO.

Another aspect that can be commented here is the effect of the air compress-

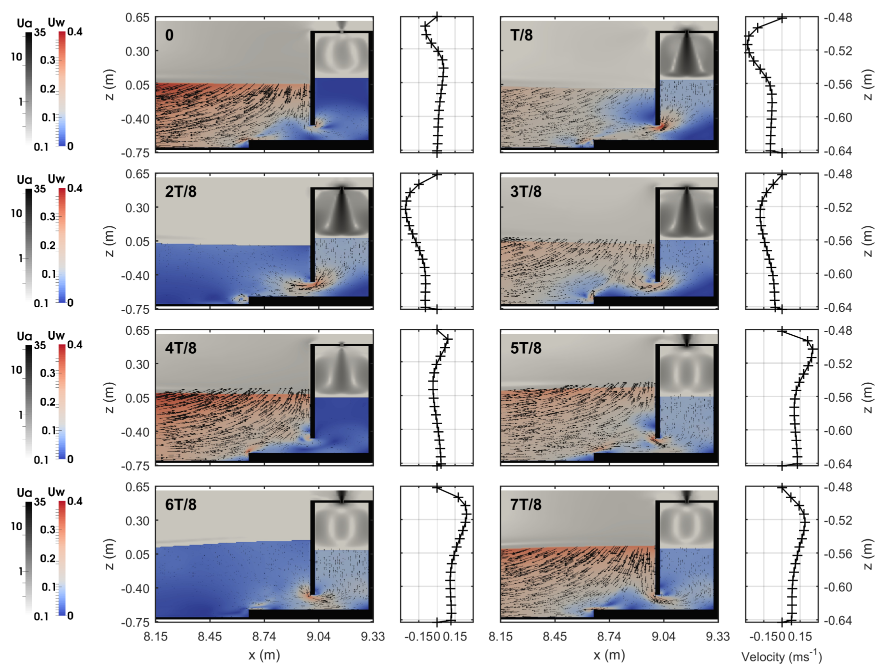

Figure 14: Velocity magnitude fields of the water and air phase inside the OWC and its vicinity every 1/8 of the wave period. The grayscale results in logarithmic scale represent the air phase (Ua) and the colour plot the water phase (Uw). The velocity profiles next to the contour plots represent the horizontal component of the velocity at the opening of the front wall.

ibility inside the chamber of the OWC for the case of very high damping. One could argue that discrepancies observed in the pressure in Figure 6b might be caused by the incompressibility assumption in the RANS model. Compressibility starts influencing the flow when entering the subsonic regime, which occurs when the ratio of the flow velocity over the speed of sound (for present conditions 340 m/s) is greater than 0.3 [31]. For the highest instantaneous velocities observed in the present study, this ratio is approximately 0.1. Therefore, the assumption of incompressibility still holds without any concerns.

In conclusion, the analysis shows that CFD models can offer valuable information for the kinematics of the two fluid phases, which can lead to better optimization of the OWC devices. A key aspect for increasing the performance [39] is the creation of a piston-type movement of the OWC, which causes the least turbulence. The kinematics can also offer information for the loading on the walls of the OWC, which is a crucial element in the structural design.

5. Conclusions

In this paper, a NWT designed in the open-source RANS-based CFD model OpenFOAM was used to replicate experimental results regarding the interaction between an OWC with regular and irregular waves. For the cases examined, very good agreement with the experiment was found for the pressure and the surface elevation inside the OWC for the regular waves and taking into account previous works with similar NWTs the model can be considered sufficiently validated. The minor discrepancies appearing in the air pressure are a common issue in similar NWTs and they are likely to be caused by the re-reflected waves from the inlet relaxation zone. For the irregular waves, the numerical and the physical model appear to have similar bulk properties regarding the hydrodynamic efficiency, response of the OWC and the reflection coefficients.

In the second part of the study, the numerical model was used for additional studies, namely the sloshing in the OWC chamber, the decay test, the performance assessment and the reflection analysis. The result of the decay test had very good agreement with the classical method for finding the performance curve and it can be used in numerical models to save significant computational effort. The OWCs appear to have less reflections than conventional vertical breakwaters and the OWC model without the PTO can be a promising alternative design of absorbing sea walls. One of the greatest strengths of the CFD model is that it can provide a valuable insight in the kinematics of the water and air in the vicinity of the device, which can be used for detailed optimization of the OWCs.

Future work should include further comparisons between the physical and the numerical model, such as the air velocities near the orifice and the loads on the walls of the OWC. An important issue that has to be tackled is the computational efficiency of the numerical model. Despite its high accuracy, a 3D CFD model is computationally expensive and difficult to apply. Future studies should exploit the capabilities of OpenFOAM to create equivalent 2D cases that will be more efficient for the preliminary studies and the long simulations with irregular waves. Moreover, since the inlet relaxation zones occupy a big part of the computational domain and the alternative of active wave absorption should also be considered [21]. Another way to decrease the computational cost is to explore different methods of simulating a PTO, so that high air velocities of the orifice are limited and the simulation does not slow down or experience instabilities. The domain decomposition and coupling of different numerical models can also be used to improve the computational efficiency [46].

References

[1] A. Clément, P. McCullen, A. Falcão, A. Fiorentino, F. Gardner, K. Hammarlund, G. Lemonis, T. Lewis, K. Nielsen, S. Petroncini, M. T. Pontes, P. Schild, B. O. Sjöström, H. C. Sø rensen, T. Thorpe, Wave energy in Europe: Current status and perspectives, Renewable and Sustainable Energy Reviews 6 (5) (2002) 405–431. doi:10.1016/S1364-0321(02)00009-6.

[2] MERiFIC, Procurement Code of Practice: A guide for businesses entering

the marine renewable energy industry, Tech. rep. (2013).
URL http://www.merific.eu/files/2011/08/WP5-2-Report-web.pdf

[3] E. Enferad, D. Nazarpour, New Developments in Renewable Energy, Intech, 2013, Ch. 12. doi:10.5772/53806.
URL http://www.intechopen.com/books/new-developments-in-renewable-energy/ocean-s-renewable-power-and-review-of-technologies-case-study-waves

[4] C. B. Boake, T. J. T. Whittaker, M. Folley, H. Ellen, Overview and Initial Operational Experience of the LIMPET Wave Energy Plant, Vol. 3, 2002, pp. 586–594.

[5] A. Pecher, J. P. Kofoed, I. L. Crom, F. Neumann, E. d. B. Azevedo, Performance assessment of the Pico OWC power plant following the EquiMar Methodology, in: Proceedings of 21st International Offshore and Polar Engineering Conference, Vol. 8, 2011, pp. 548–556.
URL http://e-book.lib.sjtu.edu.cn/isope2011/data/papers/11TPC-447Pecher.pdf

[6] A. F. O. Falcão, Modelling of Wave Energy Conversion, Tech. rep. (2013).
URL https://fenix.tecnico.ulisboa.pt/downloadFile/3779580606646/Chapter%25201%25282014%2529.pdf

[7] D. Stagonas, G. Müller, N. Maravelakis, D. Magagna, D. Warbrick, Composite seawalls for wave energy conversion: 2D experimental results, in: 3rd International Conference on Ocean Energy, Bilbao, Spain, 2010.

[8] V. Vannucchi, L. Cappietti, Wave energy estimation in four italian nearshore areas, in: ASME 2013 32nd International Conference on Ocean, Offshore and Arctic Engineering, American Society of Mechanical Engineers, 2013, pp. V008T09A007–V008T09A007.

[9] T. Hammons, Energy Potential of the Oceans in Europe and North America: Tidal, Wave, Currents, Otec and Offshore Wind, International Journal

of Power and Energy Systems 28 (4). doi:10.2316/Journal.203.2008.4.203-4142.

[10] T. Kelly, T. Dooley, J. Campbell, J. Ringwood, Comparison of the Experimental and Numerical Results of Modelling a 32-Oscillating Water Column (OWC), V-Shaped Floating Wave Energy Converter, Energies 6 (8) (2013) 4045–4077. doi:10.3390/en6084045.
URL http://www.mdpi.com/1996-1073/6/8/4045/

[11] M. Folley, T. Whittaker, Validating a spectral-domain model of an OWC using physical model data, International Journal of Marine Energy 2 (2013) 1–11. doi:10.1016/j.ijome.2013.05.003.
URL http://dx.doi.org/10.1016/j.ijome.2013.05.003

[12] R. Gervelas, F. Trarieux, M. Patel, A time-domain simulator for an oscillating water column in irregular waves at model scale, Ocean Engineering 38 (8-9) (2011) 1007–1013. doi:10.1016/j.oceaneng.2011.04.006.
URL http://dx.doi.org/10.1016/j.oceaneng.2011.04.006

[13] C. Josset, A. H. Clément, A time-domain numerical simulator for oscillating water column wave power plants, Renewable Energy 32 (8) (2007) 1379–1402. doi:10.1016/j.renene.2006.04.016.

[14] D.-Z. Ning, J. Shi, Q.-P. Zou, B. Teng, Investigation of hydrodynamic performance of an OWC (oscillating water column) wave energy device using a fully nonlinear HOBEM (higher-order boundary element method), Energy 83 (2015) 177–188. doi:10.1016/j.energy.2015.02.012.
URL http://linkinghub.elsevier.com/retrieve/pii/S0360544215001644

[15] H. Bouhrim, A. El Marjani, On Numerical Modeling in OWC Systems for Wave Energy Conversion, in: Renewable and Sustainable Energy Conference (IRSEC), 2014 International. IEEE, 2014, pp. 431–435.

[16] R. G. Coe, V. S. Neary, Review of Methods for Modeling Wave Energy Converter Survival, in: The 2nd Marine Energy Technology Symposium, Seattle, WA, 2014.

[17] P. R. Teixeira, D. P. Davyt, E. Didier, R. Ramalhais, Numerical simulation of an oscillating water column device using a code based on Navier Stokes equations, Energy 61 (2013) 513–530. doi:10.1016/j.energy.2013.08.062.
URL http://linkinghub.elsevier.com/retrieve/pii/S0360544213007512

[18] I. López, B. Pereiras, F. Castro, G. Iglesias, Optimisation of turbine-induced damping for an OWC wave energy converter using a RANS-VOF numerical model, Applied Energy 127 (2014) 105–114. doi:10.1016/j.apenergy.2014.04.020.

[19] A. Kamath, H. Bihs, Øivind A. Arntsen, Numerical modeling of power take-off damping in an Oscillating Water Column device, International Journal of Marine Energy 10 (2015) 1–16. doi:10.1016/j.ijome.2015.01.001.
URL http://dx.doi.org/10.1016/j.ijome.2015.01.001

[20] B. Bouali, S. Larbi, Contribution to the geometry optimization of an oscillating water column wave energy converter, Energy Procedia 36 (2013) 565–573. doi:10.1016/j.egypro.2013.07.065.
URL http://dx.doi.org/10.1016/j.egypro.2013.07.065

[21] P. Higuera, J. L. Lara, I. J. Losada, Realistic wave generation and active wave absorption for Navier-Stokes models. Application to OpenFOAM., Coastal Engineering 71 (2013) 102–118. doi:10.1016/j.coastaleng.2012.07.002.

[22] A. Iturrioz, R. Guanche, J. Lara, C. Vidal, I. Losada, Validation of OpenFOAM for Oscillating Water Column three-dimensional modeling, Ocean Engineering 107 (2015) 222–236. doi:10.1016/j.oceaneng.2015.07.051.

URL http://linkinghub.elsevier.com/retrieve/pii/S0029801815003649

[23] I. Simonetti, L. Cappietti, H. E. Safti, G. Manfrida, H. Matthies, H. Oumeraci, The use of OpenFOAM as a virtual laboratory to simulate Oscillating Water Column wave energy converters, in: VI International Conference on Computational Methods in Marine Engineering MARINE 2015, Rome, Italy, 2015.

[24] N. G. Jacobsen, D. R. Fuhrman, J. r. Fredsœ, A wave generation toolbox for the open-source CFD library: OpenFoam, International Journal for Numerical Methods in Fluids 70 (9) (2012) 1073–1088.

[25] T. Vyzikas, S. Deshoulières, M. Barton, O. Giroux, D. Greaves, D. Simmonds, Experimental investigation of different types of fixed Oscillating Water Column devices for wave energy generation, Renewable Energy(In review).

[26] H. Jasak, A. Jemcov, Z. Tukovic, OpenFOAM : A C ++ Library for Complex Physics Simulations, in: International Workshop on Coupled Methods in Numerical Dynamics, Dubrovnik, 2007.

[27] OpenCFD, OpenFOAM: The Open Source CFD Toolbox User Guide Version 2.1.1, Tech. rep. (2012).

[28] C. Hirt, B. Nichols, Volume of fluid (VOF) method for the dynamics of free boundaries, Journal of Computational Physics 39 (1) (1981) 201–225. doi:10.1016/0021-9991(81)90145-5.

[29] S. Brown, D. Greaves, V. Magar, D. Conley, Evaluation of turbulence closure models under spilling and plunging breakers in the surf zone, Coastal Engineering 114 (2016) 177–193. doi:10.1016/j.coastaleng.2016.04.002.
URL http://linkinghub.elsevier.com/retrieve/pii/S0378383916300400

[30] H. K. Versteeg, W. Malalasekera, An introduction to Computational Fluid Dynamics - The Finite Volume Method, 2nd Edition, Pearson Education Limited, 2007.

[31] J. Ferziger, M. Peric, Computational methods for fluid dynamics, 3rd Edition, Springer, Berlin, 2002.

[32] R. Courant, K. Friedrichs, H. Lewy, On the Partial Difference Equations of Mathematical Physics, IBM Journal of Research and Development 11 (2) (1967) 215–234. doi:10.1147/rd.112.0215.

[33] R. G. Dean, R. A. Dalrymple, Water Wave Mechanics for Engineers and Scientists, World Scientific, 1984.

[34] P. Boccotti, Caisson breakwaters embodying an OWC with a small opening - Part I: Theory, Ocean Engineering 34 (5-6) (2007) 806–819. doi:10.1016/j.oceaneng.2006.04.006.

[35] I. Simonetti, L. Cappietti, H. E. Safti, H. Oumeraci, Numerical modelling of fixed Oscillating Water Column wave energy conversion devices: Toward geometry hydraulic optimization, in: Proceedings of the ASME 34th International Conference on Ocean, Offshore and Arctic Engineering OMAE2015, St. Johns, Newfoundland, Canada, 2015.

[36] L. H. Holthuijsen, Waves in Oceanic and Coastal Waters, Cambridge University Press, 2007.

[37] T. E. Baldock, D. J. Simmonds, Separation of incident and reflected waves over sloping bathymetry, Coastal Engineering 38 (3) (1999) 167–176. doi:10.1016/S0378-3839(99)00046-0.

[38] Y. Goda, Y. Suzuki, Estimation of incident and reflected waves in random waves experiments, in: Proceedings of 15th Conference on Coastal Engineering, Vol. No 15, Honolulu, Hawaii, USA, 1976. doi:10.1016/0029-8018(93)E0011-G.

URL https://icce-ojs-tamu.tdl.org/icce/index.php/icce/article/view/3096

[39] D. Evans, R. Porter, Hydrodynamic characteristics of an oscillating water column device, Applied Ocean Research 17 (3) (1995) 155–164. doi:10.1016/0141-1187(95)00008-9.

[40] Y. Zhang, Q.-P. Zou, D. Greaves, Airwater two-phase flow modelling of hydrodynamic performance of an oscillating water column device, Renewable Energy 41 (2012) 159–170. doi:10.1016/j.renene.2011.10.011.
URL http://dx.doi.org/10.1016/j.renene.2011.10.011

[41] M. E. McCormick, Ocean Wave Energy Conversion, Dover Publications, 2007.

[42] M. T. Morris-Thomas, R. J. Irvin, K. P. Thiagarajan, An Investigation Into the Hydrodynamic Efficiency of an Oscillating Water Column, Journal of Offshore Mechanics and Arctic Engineering 129 (4) (2007) 273–278. doi:10.1115/1.2426992.

[43] R. Van't Veer, F. Fathi, On the roll damping of an FPSO with riser balcony and bilge keels, International Journal of Maritime Engineering 153 (2) (2011) 125–135. doi:10.3940/rina.ijme.2011.a2.wf7.

[44] C. W. de Silva, Vibration - Fundamental and Practice, CRC Press, 2000.

[45] N. S. Nise, Control systems Engineering - Sixth edition, John Wiley & Sons, 2010.

[46] B. T. Paulsen, H. Bredmose, H. B. Bingham, An efficient domain decomposition strategy for wave loads on surface piercing circular cylinders, Coastal Engineering 86 (2014) 57–76. doi:10.1016/j.coastaleng.2014.01.006.